Title: Nanotopography enhances dynamic remodeling of tight junction proteins through cytosolic complexes

Authors: Xiao Huang[1], Xiaoyu Shi[2,3], Mollie Eva Hansen[4], Cameron L. Nemeth[4], Anna Ceili[5], Bo Huang[2,6,7], Theodora Mauro[5], Michael Koval[8], and Tejal A. Desai[1,4]*

Affiliations:

[1] Department of Bioengineering and Therapeutic Sciences, University of California, San Francisco, San Francisco, California, USA

[2] Department of Pharmaceutical Chemistry, University of California, San Francisco, San Francisco, California, USA

[3] Department of Developmental and Cell Biology, University of California, Irvine, Irvine, California, USA

[4] UC Berkeley-UCSF Graduate Program in Bioengineering, University of California, San Francisco, San Francisco, California, USA

[5] Department of Dermatology, University of California, San Francisco, San Francisco, California, USA

[6] Department of Biochemistry and Biophysics, University of California, San Francisco, San Francisco, California, USA

[7] Chan Zuckerberg Biohub, San Francisco, California, USA

[8] Division of Pulmonary, Allergy, and Critical Care Medicine and Department of Cell Biology, Emory University School of Medicine, Atlanta, Georgia, USA

*Correspondence to: Tejal A. Desai, PhD (email: tejal.desai@ucsf.edu)

Abstract

The epithelial tight junction regulates barrier function and is responsive to extracellular stimuli. Here we demonstrated that contact of synthetic surfaces with defined nanotopography at the apical surface of epithelial monolayers increased paracellular permeability of macromolecules. To monitor changes in tight junction morphology in live cells, we fluorescently tagged the scaffold protein zonula occludens-1 (ZO-1) through CRISPR/Cas9-based gene editing. Contact between cells and nanostructured surfaces destabilized junction-associated ZO-1 and promoted its arrangement into highly dynamic non-junctional cytosolic complexes that averaged ~2 μm in diameter. Junction-associated ZO-1 rapidly remodeled, and we also observed the direct transformation of cytosolic complexes into junction-like structures. Claudin-family tight junction transmembrane proteins and F-actin also were associated with these ZO-1 containing cytosolic complexes. These data suggest that the cytosolic structures are novel intermediates formed in response to nanotopographic cues that facilitate rapid tight junction remodeling in order to regulate paracellular permeability.

Introduction

Tight junctions are protein complexes at epithelial apical intercellular contact sites, which form barriers that regulate the paracellular transit of water, ions and molecules (*1-3*). Although their barrier forming properties and morphology suggest a static structure, in fact, tight junction associated proteins are highly dynamic, and can be acutely regulated by external stimuli to alter the extent of paracellular flux (*2, 4*). In

particular, the tight junction associated scaffold protein zonula occludens-1 (ZO-1) has been shown to be an important regulator for barrier permeability (*5-9*). ZO-1 is highly mobile, and readily exchanges between tight junctions and the cytosol (*2, 4*). This dynamic process is closely associated with binding to transmembrane tight junction proteins (e.g. claudins, JAM-A) and cytoskeletal proteins, primarily actin (*5, 6, 8*). Detailed understanding of the molecular anatomy of the tight junctions as well as determining how dynamic interactions between tight junction proteins dictate barrier function continue to be elucidated (*2*).

Synthetic materials fabricated with specific geometries and surface topographic features at the micro and nanoscale have the capacity to influence epithelial cell behavior (*10, 11*). We previously found that polymeric films with defined nanostructure, when placed in contact with the apical aspect of an epithelial monolayer, led to enhanced transepithelial permeability of macromolecules ranging in size from ~60 kDa to ~150 kDa, including bovine serum albumin and IgG (*12-14*). Immunolabeling of ZO-1 showed characteristic changes in tight junction morphology that were associated with increased permeability, further indicating nanotopography-induced regulation of tight junctions (*12*). Tight junction remodeling occurs relatively quickly (within 1 hour), is reversible, energy-requiring, and depends on MLCK (myosin light chain kinase) signaling (*12, 13*). However, detailing the precise timing and changes to tight junctions that occur in response to nanostructure contact remain to be determined and require specialized methodology. Specifically, commonly used methods to detect epithelial paracellular flux, including transepithelial electrical resistance (TEER) and transepithelial diffusion through porous Transwell inserts (*15, 16*), measure bulk epithelial layer behavior and are unable to obtain submicrometer scale precision (*2*). Moreover, systems incorporating fluorescently tagged proteins-of-interest for live cell imaging are frequently subject to overexpression, which can alter physiological behavior (*1, 15, 17*).

To advance our ability to analyze the effects of nanotopography on epithelial cell permeability, we developed a novel method to achieve high-resolution visualization of paracellular flux across live cell monolayers in real time, using total internal reflection fluorescence (TIRF) microscopy, which specifically images the basal side of epithelia within ~100 nm from the glass substrate (*18*). We also tagged endogenous ZO-1 protein under the control of its endogenous promoter with mCherry using CRISPR-Cas9 based gene editing, enabling live cell tracking of morphological changes to ZO-1. Through these advanced imaging methods and fluorescence recovery after photobleaching (FRAP) assays, we identified novel nanostructure-induced dynamics of junction-associated ZO-1. This remodeling process was mediated through the formation of cytosolic structures containing ZO-1, claudin-family transmembrane tight junction proteins and F-actin that dynamically interacted with tight junctions. These ZO-1 positive cytosolic complexes are consistent with recently reported structures induced by ZO-1 phase separation that have been implicated as mediators for tight junction formation and mechanosensing (*19, 20*). Our ability to use nanotopography to stimulate active tight junction remodeling by this novel biophysical process provides a basis to understand mechanisms that regulate tight junction assembly and epithelial barrier function in response to the extracellular microenvironment.

Results

Nanotopographic cues induce paracellular flux of macromolecules across epithelial monolayers

Human epithelial colorectal adenocarcinoma (Caco-2) cells were cultured on glass-bottomed chambers under conditions that enabled them to form a polarized monolayer (**Fig. 1A**, fig. S1A). The cells were then placed in contact with polypropylene films with or without a defined nanotopographic structure (**Fig.**

87   **1B**, fig. S1B). FITC-labeled IgG (FITC-IgG) was added to the apical side of the monolayer as a tracer for
88   barrier permeability (**Fig. 1A**, fig. S1A). We then tracked FITC-IgG that penetrated through epithelial
89   monolayers to the basal side with submicron resolution, using TIRF microscopy that selectively
90   illuminated fluorophores within ~100 nm zone above the basal substrate (**Fig. 1A**). Acquired TIRF images
91   were quantified as the mean FITC fluorescence intensity at cell-cell borders marked by bulk plasma
92   membrane using Cell Mask Deep Red (fig. S1C). Strikingly, FITC-IgG accumulated in basolateral gaps
93   below cell-cell borders of Caco-2 monolayer after apical contact with nanostructured (NS) films for 1
94   hour at 37°C (**Fig. 1, C and D**), while FITC-IgG showed minimal paracellular permeability in non-treated
95   (NT) cells (fig. S1 D and E). NS film treated cells also showed significantly higher paracellular
96   accumulation of FITC-IgG than cells in contact with control flat (FT) polypropylene films (**Fig. 1C-E**).
97   These data are consistent with our previous studies, which demonstrate increased paracellular permeability
98   to macromolecules when epithelial cells are in contact with nanotopographic structures (*12-14*), further
99   indicating the regulation of tight junctions through nanostructure contact. We then immunostained ZO-1
100 in differentially treated cells (fig. S1F**)** given its important role in tight junction regulation (*5-9*). We found
101 NS-specific effects on ZO-1 morphology, including induction of a zigzag appearance in the xy focal plane
102 (**Fig. 1, F and G**) and xz/yz focal plane (fig. S1, G and H), and interestingly, a novel class of cytosolic
103 complexes (**Fig. 1, F and H**).

Live cell imaging reveals cytosolic tight junction protein complexes induced by contact with nanostructured films

106 Considering NS-induced morphological changes in ZO-1 (**Fig. 1, F to H**) and its important role in tight
107 junction regulation (*8, 9*), we engineered cells using CRISPR-Cas9 based genome editing to express ZO-
108 1 tagged at the N terminus with a fluorescent reporter (mCherry) for live cell imaging. Using this approach,
109 the ZO-1 was precisely tagged and endogenously expressed, thus maintaining its physiological activity
110 (*21*) (**Fig. 2A**). Briefly, the guide RNA (gRNA) was designed to target exon2 of *TJP1* gene for site specific
111 insertion/deletion (indel) (fig. S2A). Thereafter, the *mCherry* gene with two 1kb arms homologous to the
112 indel site was integrated into the genome through homology directed repair (HDR) (**Fig. 2A**). Transduced
113 Caco-2 cells were selected for mCherry expressing cells through fluorescence-activated cell sorting
114 (FACS) (fig. S2B), followed by single clone isolation and genomic PCR confirmation (fig. S2C). The 19
115 clones we isolated were all heterozygous with only one allele modified (fig. S2C). Isolated clones cultured
116 on Transwells were used for phenotypic confirmation. Based on TEER analysis, clone15 had barrier
117 function comparable to wildtype cells and thus was used for detailed imaging analysis (fig. S2D).
118 Noticeably, live imaging and z-stack scanning of engineered cells showed the existence of cytosolic
119 mCherry-tagged ZO-1 complexes near tight junctions, mostly adjacent to the apical surface (fig. S2F).

120 Live cells expressing mCherry-ZO-1 at physiological levels were highly susceptible to photobleaching.
121 To minimize this effect, a spinning disk confocal microscope with high imaging speed was used for live
122 cell imaging, where mCherry-ZO-1 fluorescence was collected at an apical 1 μm z-depth with 0.3 μm
123 intervals and z-projected at maximum pixel intensity for each time lapse image (**Fig. 2C**). Physical drift
124 and vibration effects were minimized during live cell imaging using the Nikon Perfect Focus System
125 (PFS). Interestingly, we observed the existence of relatively large cytosolic ZO-1 containing structures
126 (~2 μm) at the apical side next to tight junctions when cells were in contact with NS films, whereas
127 untreated cells and cells treated with FT films showed fewer and smaller cytosolic ZO-1 complexes (**Fig.**
128 **2C**). We quantified (*22*) cytosolic structures in 40 μm x 40 μm apical images from 5 independent
129 experiments (fig. S3A), and found a significantly higher number of large cytosolic ZO-1 complexes (d ≥
130 1 μm) in NS film-treated cells compared to untreated or FT film-treated cells (**Fig. 2, D and E**). To
131 investigate their composition, we immunostained differentially treated cells for several markers, including

132 ZO-1, claudins, F-actin and the endocytosis marker Rab5. mCherry positive apical cytosolic structures
133 were confirmed to be ZO-1 positive, and also co-localized with several claudins (Claudin-2, -4, -10) and
134 F-actin (**Fig. 2F,** fig. S3, B and C). Notably, the structures were negative for Rab5 staining (fig. S3C), and
135 were non-acidic based on a lack of LysoTracker staining (fig. S3D), indicating that they did not originate
136 from vesicular mediated trafficking of endocytosed tight junction proteins.

Enhanced dynamics of tight junction remodeling stimulated by nanotopography

138 We investigated the dynamics of mCherry-ZO-1 remodeling, using time-lapse imaging of Caco-2 cells
139 stimulated by nanotopography. We observed two patterns of cytosolic structure initiation: i) the direct
140 transition of junction-associated ZO-1 into cytosolic structures through aggregation and departure (**Fig.**
141 **3A-i**); ii) the clustering of diffused signals into puncta within a network next to tight junctions (**Fig. 3A-**
142 **ii,** see movie S1). In addition, the cytosolic structures became enlarged through fusion of newly formed
143 small structures (**Fig. 3A-iii**). Interestingly, cytosolic structures were highly dynamic in that they were
144 observed to circulate apically while collecting more ZO-1 followed by movement toward the basal aspect
145 of the cytoplasm (**Fig. 3A-iv**, see movie S2 and movie S3). On the other hand, we also observed the rapid
146 reorganization of ZO-1 into junction-like structures that often originated from non-apical locations (**Fig.**
147 **3A-i,v**). Occasionally, we saw direct conversion of spherical structures into junction-like structures (**Fig.**
148 **3A-vi**). With TIRF imaging, we also observed ZO-1 positive junction-like structures at the basal side of
149 Caco-2 monolayer stimulated by apical contact with nanotopography (fig. S4A**).** The appearance of basal
150 ZO-1 positive strands suggests that apical contact with NS films may induce cells to reorient their apical-
151 basolateral axis.

152 In contrast, we did not observe active ZO-1 remodeling in cells that were either untreated or in contact
153 with FT films, where instead there was minimal interaction between tight junctions and apical cytosolic
154 structures, Moreover, there were fewer and smaller ZO-1 positive cytosolic complexes in cells that were
155 not NS-treated (fig. S4, B and C).

156 We then used FRAP at selected regions to quantify and compare the remodeling rate of tight junctions in
157 response to NS contact (**Fig. 3B**). Importantly, we found that mCherry-ZO-1 fluorescence at tight
158 junctions recovered faster after photobleaching in cells stimulated by NS films, as compared to untreated
159 cells and FT film treated cells (**Fig. 3C**). This further supports that there is enhanced remodeling of
160 junctional ZO-1 being induced by nanotopographic cues.

161 To examine the dynamics of a transmembrane tight junction protein in live cells, we transfected mCherry-
162 ZO-1 expressing Caco-2 cells with exogenous YFP-claudin-3 using an adenovector expression construct
163 (*23*) (**Fig. 4A**). The virus titer was optimized to minimize YFP-claudin-3 overexpression although this did
164 result in heterogeneous expression by different cells in the monolayer (**Fig. 4B**). YFP-claudin-3 and
165 mCherry-ZO-1 co-localized at apical cytosolic structures in NS film-treated cells (**Fig. 4B**), but not
166 untreated cells or FT film-treated cells (fig. S5). Importantly, claudin-3 was present in ZO-1 containing
167 cytosolic structures at sites of formation and sites of interaction with tight junctions (**Fig. 4, C and D**, see
168 movie S4). The co-localization of the transmembrane tight junction protein claudin-3 with cytosolic
169 scaffold protein ZO-1 indicates that cytosolic complexes involve the regulation of multiple classes of tight
170 junction proteins, including transmembrane proteins.

171

F-actin engages during the formation of cytosolic tight junction complexes

173 ZO-1 interconnects transmembrane junction proteins (e.g. claudins) and cytoskeletal F-actin in epithelial
174 cells (*5, 6*). We imaged F-actin labeled with SiR-actin in live cells under NS and FT film treatment, to

175 investigate the changes in cytoskeletal morphology in response to different stimuli (**Fig. 5A**). We observed
176 apparent clustering of F-actin in cells upon NS film treatment as opposed to untreated cells or FT film
177 treated cells. These clusters formed in response to NS contact translocated from the apical aspect of the
178 cells to the basal side over 1.5 hour (fig. S6A). More specifically, F-actin interacted with ZO-1 proteins
179 during tight junction remodeling in different ways (see movie S5): i) F-actin replaced sites of ZO-1 protein
180 localization at tight junctions (**Fig. 5B-i**); ii) F-actin intertwined with ZO-1 in cytosolic complexes sitting
181 next to tight junctions (**Fig. 5B-ii**); iii) polarized cytosolic F-actin-ZO-1 structures (**Fig. 5B-iii**) with the
182 F-actin portion facing towards iv) larger solid integrated structure (**Fig. 5B-iv**); and v) F-actin and ZO-1
183 co-localized in large (>2 μm) hollow structures (**Fig. 5B-v**). In some instances, F-actin:ZO-1 containing
184 structures merged into larger co-localized structures (**Fig. 5C**). And interestingly, there were instances
185 where F-actin dissociated from ZO-1 containing cytosolic structures (**Fig. 5, D and E**). Consistent with
186 this, cytosolic structures containing both ZO-1 and Claudin-3 lacked F-actin (**Fig. 5, F and G**), indicating
187 that interactions of F-actin with cytosolic complexes are transient and F-actin dissociates as the complexes
188 mature.

189 Taken together, our data support the hypothesis that NS materials in direct contact with the apical surface
190 of epithelial cells induce F-actin rearrangements. The rearrangements are coordinated with changes in
191 localization and morphologies of its binding partner, ZO-1. Transition of junction-associated ZO-1 into
192 large cytosolic complexes also recruit other tight junction proteins, suggesting a new mechanism of tight
193 junction regulation by biophysical stimuli (**Fig. 5H**).

194

Discussion

196 Tight junctions, comprised of heavily cross-linked complexes of transmembrane and membrane-
197 associated proteins, represent a structural determinant of epithelial cell polarity and regulate solute
198 paracellular permeability (*1, 3*). Tight junctions are highly dynamic, even in unstimulated cells, and are
199 acutely regulated by multiple extracellular biological stimuli including hormones and cytokines (*2, 4*). We
200 previously found *in vitro* and *in vivo* that cell contact with polymeric films with defined nanotopographic
201 features enhances transepithelial permeability to macromolecules in the size range of (60 kDa to 150 kDa)
202 (*12-14*). Here, for the first time, we used state-of-the-art TIRF microscopy to visualize paracellular flux
203 of FITC-labeled IgG with submicron resolution at the basal aspect of live epithelial monolayers stimulated
204 with a nanostructured biophysical cue on the apical surface. The ability to image transepithelial flux in
205 live cell monolayers provided more detailed morphological information than methods measuring bulk
206 solute flow and enabled us to demonstrate that the paracellular route is a major pathway for nanostructure-
207 induced transepithelial permeability.

208 ZO-1 has been shown to play an essential role in the maintenance and regulation of tight junction
209 permeability (*8, 9, 20*). To track the intracellular distribution of ZO-1 in live cells, we used CRISPR-Cas9
210 based gene editing to attach a fluorescent mCherry reporter to the N-terminus of endogenous ZO-1.
211 Engineered ZO-1 expression was driven by its endogenous promoter which ensured that it was expressed
212 and regulated at physiologically relevant concentrations avoiding pitfalls related to overexpression (*1, 19*).
213 Live imaging and FRAP analysis of cells triggered by nanostructured films revealed a change in the
214 kinetics of ZO-1 turnover associated with the response of tight junctions to the contact between cells and
215 NS films. Our findings also are consistent with previous studies demonstrating that tight junction
216 associated ZO-1 is highly mobile and exchanges with the cytosolic pool (*2, 4*). Furthermore, the imaging
217 methods used here also enabled us to identify a novel intermediate involved in nanostructure-induced
218 remodeling tight junctions, namely, large (~2 μm diameter) cytosolic ZO-1-containing complexes that co-
219 localize with claudin-family proteins and, in some cases F-actin. This ZO-1 positive cytosolic structure

220 has the characteristics of a newly described complex that forms as a result of liquid-liquid phase separation
221 of ZO-1 (*19*). Phase separation of ZO-1 and its accompanied junctional proteins was also reported as an
222 important intermediate for tight junction assembly (*19*) and mechanosensing (*20*). Here we extend these
223 observations by showing that a nanostructured surface with the capacity to increase transepithelial
224 permeability also induces the formation of ZO-1 positive cytosolic complexes in conjunction with an
225 increase in tight junction remodeling. In addition, the previous studies demonstrated the formation of
226 liquid-liquid phase separated ZO-1 complexes in cell free systems and cells overexpressing ZO-1 (*19*).
227 Critically, the engineered cells we examined expressed comparable, physiologic levels of mCherry-ZO-1
228 as untagged ZO-1, thus demonstrating the formation of these complexes can occur in response to a
229 physiologic stimulus and was not driven by protein overexpression.

230 ZO-1 is a peripheral tight junction protein that interconnects transmembrane tight junction proteins (e.g.
231 claudins, occludin, JAM) and F-actin (*5, 6*). Based on structure-function analysis, ZO-1 phase separation
232 was attributed to the unfolding of the PSG (PDZ-SH3-GuK) domain, which is directly regulated by
233 binding to the F-actin cytoskeleton (*7, 9, 19*). Moreover, it has been previously shown that ZO-1 positive
234 cytosolic complexes are associated with the actin cytoskeleton that facilitated their delivery to nascent
235 tight junctions in response to changes in tension that occur during gastrulation (*20*). Consistent with this
236 model, we also observed that F-actin transiently interacted with cytosolic structures in response to
237 nanotopography. A role for tension in the formation of ZO-1 cytosolic complexes is also suggested by the
238 observation that integrin stimulation is required for nanotopography-induced epithelia permeability (*12,*
239 *13*). We also found that ezrin, a cytosolic scaffold protein that links the actin cytoskeleton to cellular
240 membrane receptors (*24*), was upregulated in NS-treated cells (fig. S6B). Thus, a signal transduction
241 pathway from membrane receptors to ezrin, F-actin, ZO-1, and then to other junctional proteins, may
242 transduce physical signals from cell apical contacts to modulate tight junction function. This agrees with
243 the recent work demonstrating that ZO-1 phase separation mediates mechano-sensing of tight junctions
244 (*20*).

245 In summary, we have developed a series of advanced imaging methods that enabled the visualization of
246 transepithelial penetration at submicron resolution and the analysis of tight junction protein dynamics in
247 live cells. Using these approaches, we found that there were hallmark changes in ZO-1 trafficking that
248 were associated with increased paracellular permeability of macromolecules induced by nanotopographic
249 cues. Of particular interest, our data demonstrate that unique ZO-1 containing cytosolic complexes can be
250 induced to interact with tight junctions to regulate their permeability. Our data also underscore that
251 nanotopography is a unique stimulus for fast and reversible modulation without permanent loss of
252 epithelial monolayer integrity. In addition, the imaging techniques shown here have general applicability
253 to understanding the mechanistic basis for tight junction permeability and how barrier function can be
254 modulated by other stimuli in real time at the level of individual intercellular junctions.

255
256
257 **Materials and Methods**

258 **Cell lines and culture**

259 Caco-2 human colon epithelial cell line was purchased from ATCC (#HTB-37). Unless specified, cells
260 were cultured in DMEM (Sigma, #D5796) supplemented with 20% FBS (Gemini Bio #100-106), 100 mM
261 sodium pyruvate (Sigma #113-24-6), and penicillin-streptomycin (Sigma #516106) incubated in 5% CO_2
262 at 37°C. The cells were subcultured at 90% confluency by trypsinization with 0.25% trypsin-EDTA (SM-
263 2003). For transepithelial electrical resistance (TEER) measurements, cells were seeded in a 6.4 mm
264 Transwell inserts (Corning #353495) with 300 μL medium containing 84,000 cells/cm^2 seeded in the

265 upper chamber and 500 μL medium in the bottom chamber. The medium was replenished every other day,
266 and TEER was measured using a voltohmmeter (World Precision Instruments) from day 6-16 where the
267 measured resistance in Ohms was multiplied by the area of the Transwell filter (0.3 cm^2). For live cell
268 imaging, 200,000 cells were seeded on a 35 mm glass bottom dish with 14 mm micro-well #0 cover glass
269 (Cellvis #D35-14-0-N), which was precoated with 0.3 mg/mL Matrigel (Corning #354234) at 37°C for 30
270 minutes. Cell culture medium was replenished every other day. After 8-10 days, the monolayer was
271 exchanged with cell imaging medium containing FluoroBrite DMEM Media (Thermo #A1896701) and
272 20% FBS for live cell imaging analysis.

CRISPR/Cas9 knock-in in Caco-2 cells

274 To generate an N-terminal mCherry knock-in in the initial exon of ZO-1, guide RNA (gRNA) for
275 CRISPR/Cas9 mediated site-specific gene editing was designed using Benchling CRISPR tool
276 (www.benchling.com).   gRNA   targeting   *TJP1*   gene   exon   number   2   -
277 5'CCTTTATCAGAGCACAGCAA3' was synthesized and complexed with trans-activating crRNA by
278 IDT. 500,000 Caco-2 cells were suspended in 100 μL buffer (Lonza #VCA-1002) supplemented with 264
279 pmol gRNA duplex, 10 μg Cas9 expression plasmid (GE Healthcare #U-005100-120), and 10 μg repair
280 plasmid (Genscript, Note S1), followed by electroporation using program B024 of Nucleofector^{TM} 2b
281 Device (Lonza #AAB-1001). Cells were then plated in one well within a 24-well plate supplemented with
282 1 mL medium. To validate CRISPR/Cas9 and gRNA mediated site-specific insertion/deletion (indel), cells
283 from the transfection without repair plasmid were collected after 3 days for genome extraction (Bioline
284 #BIO-52066)   and   PCR   (NEB   #M0491S)   at   the   region   of   indel   (forward   primer:
285 5'TGTTTGTGACGTTAAAGCAGCC3', reverse primer: 5'CACAAACTTACCCTGTGAAGCG3').
286 Genome indel was assessed by T7 Endonuclease I assay (NEB #M0302) followed by SDS-PAGE gel
287 electrophoresis (Genscript #M42012L). Seven days after the transfection of the complex including the
288 repair plasmid, cells were collected and sorted by FACS (Sony SH800) for enrichment of mCherry
289 positive cells. Enriched cells were plated and subcultured in 10 cm dishes at 3000 cells per dish to produce
290 single cell clones. Nineteen clones were isolated after 2 weeks, further expanded, and confirmed for
291 mCherry knock-in through genome extraction, PCR (using the same primer pair as above) and analyzed
292 by agarose gel electrophoresis.

Nanostructured film fabrication and cell treatment

294 Nanostructured films were made, as previously described (*12-14*), by nanoimprint lithography in which
295 polypropylene was heated above its glass transition temperature and pressed into a silicon mold. Molds
296 were fabricated using electron beam lithography followed by anisotropic reactive ion etching to generate
297 precise submicron structures. Nanostructured films were characterized using a Phenom scanning electron
298 microscope (SEM). Nanostructured films or flat (unstructured) films (outside of the imprinted region)
299 were biopsy punched into 6 mm diameter circles, the backside of which was glued to a polyethylene
300 terephthalate film with a 0.3-inch of pipette tip attached. This device was placed in direct contact with a
301 cell monolayer on the apical side and precision weighted with two metal rings of ~0.2 g and used for cell
302 studies.

TIRF microscopy for paracellular flux analysis

304 Caco-2 cell monolayers, cultured on glass-bottom tissue culture dishes, were stained for plasma
305 membranes (CellMask Deep Red Stain, 5 μg/mL, Thermo #C10046) and nuclei (Hoechst 33342, 5 μg/mL,
306 Thermo #H3570) at 37°C for 10 mins in DMEM medium without FBS, followed by two rinses using cell
307 imaging medium. An NS (nanostructured) or FT (flat) film device was placed in contact with cells on
308 apical side along with FITC-IgG (Sigma #F9636) supplemented to the cell imaging medium at 10 μg/mL.

309 After 1 h incubation at 37ºC, live cells were imaged using an OMX-SR microscope (GE Health Care) in
310 the ring-TIRF mode equipped with PCO Edge 5.5 cMOS cameras, 4-line laser launch 405/488/568/60nm
311 (Toptica), and live cell chamber at 37° with 5% CO_2. Images were acquired using a Plan ApoN 60x/1.42
312 (Olympus) oil immersion objective with laser liquid 1.518 (Cargile), and filter sets for DAPI (435/31),
313 GFP (528/48), mCherry (609/37) and Cy5 (683/40). Registration alignment was determined using an
314 image registration target slide (GE Health Care, pat #52-852833-000) and processed with SoftWoRx 7.0.0.
315 software (GE Health Care). To quantify paracellular permeability of FITC-IgG, cell-cell border area in
316 each image was outlined by a mask, generated using signals from plasma membrane stain, using Fiji
317 software. Mean pixel intensity of FITC signal was analyzed within mask-identified area.

Confocal microscopy of live Caco-2 cells

319 Caco-2 cells were fluorescently labeled for different proteins and cell machineries as specified before live
320 cell film device treatment and imaging. For fluorescence tagging of claudin-3, adenovirus carrying YFP-
321 claudin-3 gene were prepared as described (23), and added to Caco-2 cells at ~100 MOI (multiplicity of
322 infection) 2 days prior to imaging. Adenovirus containing medium was removed by fresh medium
323 exchange one day after infection. For F-actin staining, SiR-actin (Cytoskeleton, #CY-SC001) was added
324 into the medium at 0.2 μM the day before imaging, and the medium was replenished with the imaging
325 medium right before imaging. For lysosome staining, LysoTracker Blue (Invitrogen #L7525) was added
326 to the cell culture medium at 60 nM and incubated for 1 h at 37ºC, followed by the imaging medium
327 replenishment prior to imaging. Live cell images were acquired within 90 minutes after the treatment of
328 film device, on a spinning disk confocal microscope (Nikon Ti inverted microscope with Andor Borealis
329 CSU-W1 spinning disk and Andor Zyla 4.2 sCMOS camera) equipped with Plan Apo VC 100x/1.4
330 (Olympus) oil immersion objective, 4-line laser launch 405/488/561/640nm (Andor), and live cell
331 chamber at 37° with 5% CO_2. The microscope was controlled using micro-manager, and the Nikon Perfect
332 Focus System was used to adjust for axial focus fluctuations.

Fluorescence recovery after photobleaching (FRAP)

334 FRAP experiments in cells were carried out using the Nikon spinning disk confocal microscope described
335 above with the following settings. Each regions of interest (ROI), less than 10 μm x 10 μm, was bleached
336 using a 473 nm diode with 30 mW at the back focal plane of the objective with 10 repeats. Several
337 junctions within the field of view were bleached but only one junction per cell. Pre-bleach and post-bleach
338 images were acquired with a 561 nm laser with 30 mW and 300 ms exposure. Fluorescence recovery of
339 mCherry was monitored for 200 s with a time resolution of 20 s. Mean fluorescence intensity (MFI) of
340 the bleached area was quantified by Fiji software, and cell movements during the recovery were corrected
341 by manual adjustment. Image groups were blinded for the analyzer during the quantification. Relative
342 FRAP efficiency was calculated using the following formula (t: time point, BB: before bleach, AB: after
343 bleach), and compared among different treatment groups: NT (non-treated), FT (flat), and NS
344 (nanostructured).

345
$$\% \text{ Recovery} = \frac{\text{MFI(t)} - \text{MFI (AB)}}{\text{MFI (BB)} - \text{MFI (AB)}} \times 100\%$$

Quantification of cytosolic complexes

347 A 40 μm x 40 μm frame that covers cell apical side with tight junctions in each image was selected and
348 the cytosolic ZO-1 complexes were quantified using ImageJ with following steps (22). The image was
349 first applied a median-blur filter to reduce noise, followed by segmentation of cytosolic structures using
350 the interactive h-maxima watershed tool, where parameters including seed dynamics, intensity threshold,

351 and peak flooding, were optimized and kept constant for images across treatments within the same
352 independent experiment. The binary image generated from the watershed results included the majority of
353 cytosolic structures and a portion of tight junctions as well. Thereafter, the particle analysis function was
354 used to isolate spherical cytosolic structures and report size distribution. Image groups were blinded for
355 the analyzer during the quantification.

Immunostaining

357 Caco-2 cells on tissue culture dishes were rinsed with PBS (with Ca^{2+} and Mg^{2+}) three times, and fixed at
358 room temperature in 2% paraformaldehyde/PBS (Electron Microscopy Sciences #RT-15710) for 15
359 minutes. Cells were then washed once with PBS and residual paraformaldehyde was quenched using 1M
360 glycine (Sigma #50046) in PBS for 10 minutes. Each of the following wash steps were carried out at room
361 temperature for 5 minutes. After three washes using PBS, cells were further fixed/permeabilized using
362 methanol/acetone solution (v/v:50/50) for exactly 2 minutes at room temperature. Cells were then
363 sequentially washed three times with PBS, once with 0.5% Triton^{TM}X-100 in PBS, and twice with 2%
364 goat serum (Sigma #G9023) and 0.5% Triton^{TM}X-100 in PBS. Primary antibodies including anti-ZO-1
365 (Thermo #339188), anti-Claudin-2 (#ab53032), anti-Claudin-4 (Abcam #53156), anti-Claudin-10
366 (Thermo #38-8400), anti-Rab5 (Abcam #ab18211) and anti-Ezrin (Abcam #ab4069) were used for
367 specific immunostaining, and cells were stained for 1 hour at room temperature in PBS with 2% goat
368 serum and antibody supplemented, followed by three washes using PBS with 2% goat serum. Cells were
369 then stained with secondary antibodies including goat anti-mouse-Alexa Fluor 488 (Thermo #A11029)
370 and goat anti-rabbit-Alexa Fluor 633 (Thermo #A21070) in PBS with 2% goat serum at room temperature
371 for 1 hour. For F-actin staining after fixation, Alexa Fluor 488 Phalloidin was added into the secondary
372 antibody staining mixture. Cells were washed three times with PBS followed by imaging using the
373 spinning disk confocal microscope described above.

Statistical analysis

375 All data are expressed as the mean ± the standard deviation (SD). The value of n and what n represents
376 (e.g., number of images, experimental replicates, or independent experiments) is stated in figure legends
377 and results. Statistical analysis was performed in Prism 8 (GraphPad Inc.), and the statistical test used is
378 indicated in the relevant figure legend.

379

References

381

382 1.   E. Steed, M. S. Balda, K. Matter, Dynamics and functions of tight junctions. *Trends in cell biology*
383   **20**, 142-149 (2010).
384 2.   L. Shen, C. R. Weber, D. R. Raleigh, D. Yu, J. R. Turner, Tight junction pore and leak pathways:
385   a dynamic duo. *Annual review of physiology* **73**, 283-309 (2011).
386 3.   J. M. Anderson, C. M. Van Itallie, Physiology and function of the tight junction. *Cold Spring Harb*
387   *Perspect Biol* **1**, a002584 (2009).
388 4.   L. Shen, C. R. Weber, J. R. Turner, The tight junction protein complex undergoes rapid and
389   continuous molecular remodeling at steady state. *The Journal of cell biology* **181**, 683-695 (2008).
390 5.   M. A. Odenwald *et al.*, The scaffolding protein ZO-1 coordinates actomyosin and epithelial apical
391   specializations in vitro and in vivo. *J Biol Chem* **293**, 17317-17335 (2018).
392 6.   A. S. Fanning, B. J. Jameson, L. A. Jesaitis, J. M. Anderson, The tight junction protein ZO-1
393   establishes a link between the transmembrane protein occludin and the actin cytoskeleton. *J Biol*
394   *Chem* **273**, 29745-29753 (1998).

7. L. S. Rodgers, M. T. Beam, J. M. Anderson, A. S. Fanning, Epithelial barrier assembly requires coordinated activity of multiple domains of the tight junction protein ZO-1. *J Cell Sci* **126**, 1565-1575 (2013).

8. D. Yu *et al.*, MLCK-dependent exchange and actin binding region-dependent anchoring of ZO-1 regulate tight junction barrier function. *Proceedings of the National Academy of Sciences of the United States of America* **107**, 8237-8241 (2010).

9. D. Spadaro *et al.*, Tension-Dependent Stretching Activates ZO-1 to Control the Junctional Localization of Its Interactors. *Curr Biol* **27**, 3783-3795 e3788 (2017).

10. C. B. Fox *et al.*, Micro/nanofabricated platforms for oral drug delivery. *J Control Release* **219**, 431-444 (2015).

11. L. V. Le, M. A. Mkrtschjan, B. Russell, T. A. Desai, Hang on tight: reprogramming the cell with microstructural cues. *Biomed Microdevices* **21**, 43 (2019).

12. K. R. Kam *et al.*, Nanostructure-mediated transport of biologics across epithelial tissue: enhancing permeability via nanotopography. *Nano Lett* **13**, 164-171 (2013).

13. L. Walsh *et al.*, Nanotopography facilitates in vivo transdermal delivery of high molecular weight therapeutics through an integrin-dependent mechanism. *Nano letters* **15**, 2434-2441 (2015).

14. T. Stewart *et al.*, Calibrated flux measurements reveal a nanostructure-stimulated transcytotic pathway. *Exp Cell Res* **355**, 153-161 (2017).

15. M. S. Balda *et al.*, Functional dissociation of paracellular permeability and transepithelial electrical resistance and disruption of the apical-basolateral intramembrane diffusion barrier by expression of a mutant tight junction membrane protein. *The Journal of cell biology* **134**, 1031-1049 (1996).

16. B. Srinivasan *et al.*, TEER measurement techniques for in vitro barrier model systems. *J Lab Autom* **20**, 107-126 (2015).

17. K. M. McCarthy *et al.*, Inducible expression of claudin-1-myc but not occludin-VSV-G results in aberrant tight junction strand formation in MDCK cells. *Journal of cell science* **113 Pt 19**, 3387-3398. (2000).

18. A. L. Mattheyses, S. M. Simon, J. Z. Rappoport, Imaging with total internal reflection fluorescence microscopy for the cell biologist. *J Cell Sci* **123**, 3621-3628 (2010).

19. O. Beutel, R. Maraspini, K. Pombo-Garcia, C. Martin-Lemaitre, A. Honigmann, Phase Separation of Zonula Occludens Proteins Drives Formation of Tight Junctions. *Cell* **179**, 923-936 e911 (2019).

20. C. Schwayer *et al.*, Mechanosensation of Tight Junctions Depends on ZO-1 Phase Separation and Flow. *Cell* **179**, 937-952 e918 (2019).

21. F. K. Riesen, B. Rothen-Rutishauser, H. Wunderli-Allenspach, A ZO1-GFP fusion protein to study the dynamics of tight junctions in living cells. *Histochem Cell Biol* **117**, 307-315 (2002).

22. J. M. Brazill, Y. Zhu, C. Li, R. G. Zhai, Quantitative Cell Biology of Neurodegeneration in Drosophila Through Unbiased Analysis of Fluorescently Tagged Proteins Using ImageJ. *Jove-J Vis Exp*, (2018).

23. L. A. Mitchell, C. E. Overgaard, C. Ward, S. S. Margulies, M. Koval, Differential effects of claudin-3 and claudin-4 on alveolar epithelial barrier function. *American journal of physiology* **301**, L40-49 (2011).

24. F. C. Tsai *et al.*, Ezrin enrichment on curved membranes requires a specific conformation or interaction with a curvature-sensitive partner. *Elife* **7**, (2018).
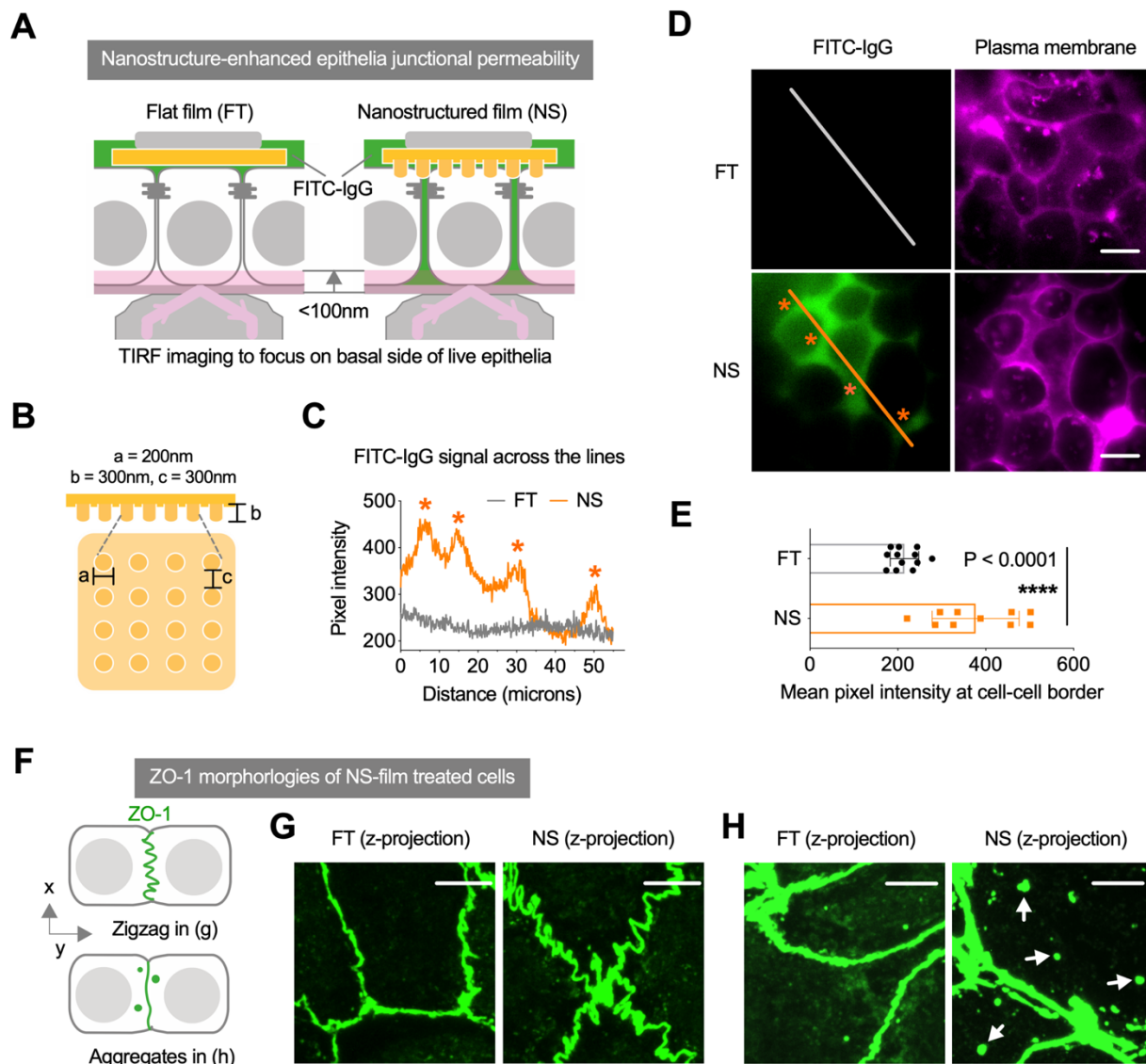
Acknowledgments

451
452

Figures

Fig. 1. **Enhanced permeability of epithelial monolayer barriers through paracellular junctions induced by contact with nanotopographic surfaces.** (**A**) Schematic of live epithelial cell basal imaging using total internal reflection fluorescence (TIRF) microscopy to track penetration of fluorescently labeled IgG. (**B**) Schematic of topographic profile of nanoimprinted polypropylene film generated from molds using electron-beam lithography. (**C**) TIRF images of the basal aspect of live Caco-2 monolayers treated with flat (FT) or nanostructured (NS) films together with FITC-labeled IgG (green) applied to the apical side for 1 hour at 37°C (from n = 3 independent experiments). The pattern of FITC-IgG accumulation at the basal side of cells treated with NS films correlated well with basolateral gaps as delineated by cell membrane staining (pink), indicating paracellular permeability. Scale bar: 10 μm. (**D**) Transverse profile of FITC-IgG as indicated by the lines in (C), showing the accumulation of FITC-IgG at basolateral gaps due to NS film treatment. (**E**) Mean fluorescence intensity of FITC-IgG at below cell-cell contact sites in (C). Data are mean ± s.d. (n = 10 images), and the *P* value was determined by two-tailed unpaired *t* test. (**F**) Schematic of ZO-1 morphological changes due to direct contact with NS films. (**G,H**) Confocal

469   microscope images of immunostained ZO-1 in Caco-2 cells treated with NS or FT film for 1 hour at 37°C,
470   showing zigzag and aggregate morphologies (white arrows) induced by nanostructures. Images are
471   projections of maximum pixel intensity of z-stack images acquired with 6 μm depth and 0.3 μm intervals.
472   Scale bar: 5 μm.
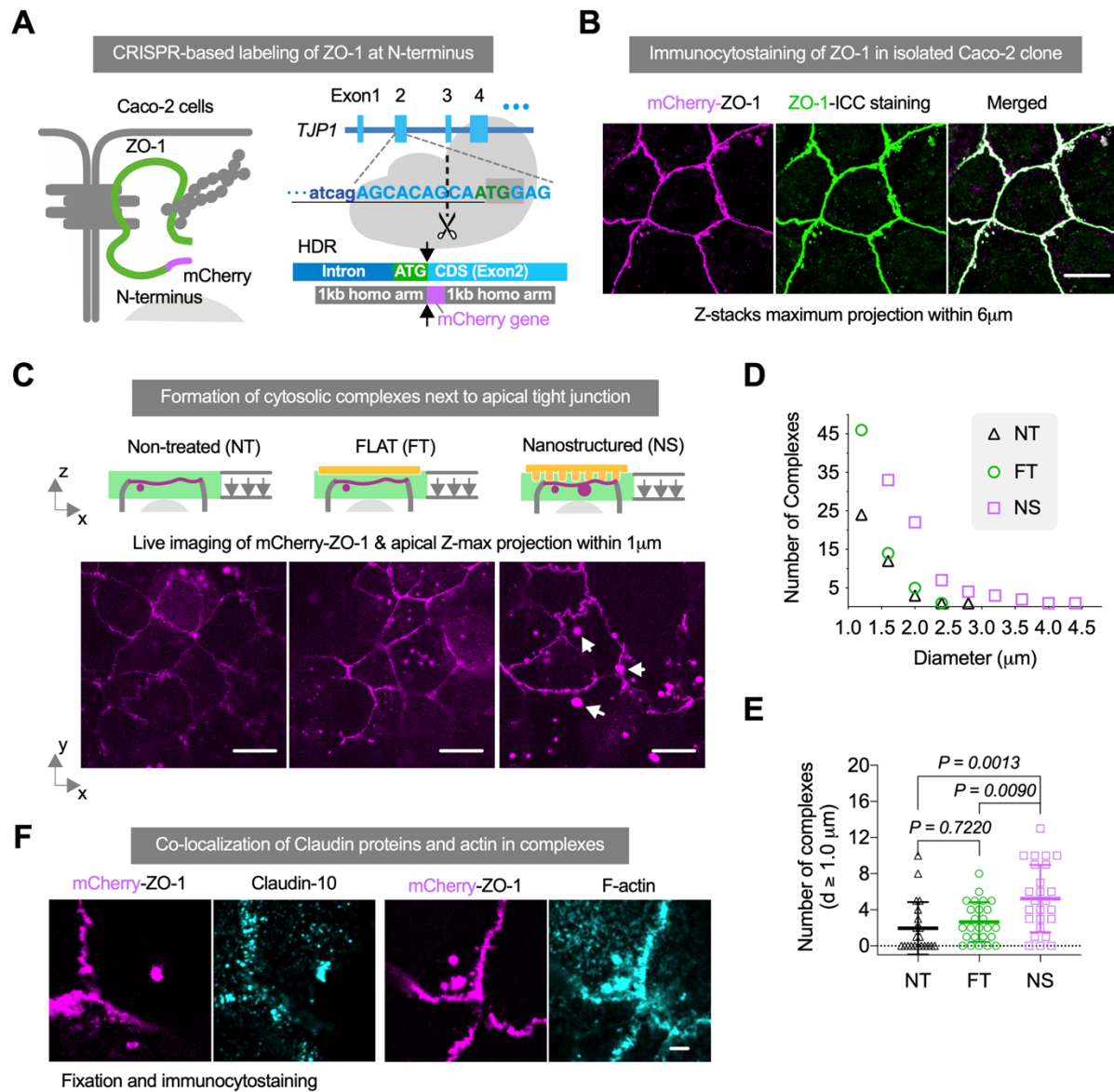
Fig. 2. Cytosolic complexes of ZO-1 induced by nanostructures, which also contain claudin-family transmembrane proteins. (**A**) Schematic of CRISPR-based tagging of mCherry reporter to the ZO-1 N-terminus under control of the endogenous promoter. The *mCherry* gene was inserted into exon2 of *TJP1* gene through homology-directed repair (HDR). (**B**) Co-localization of mCherry and immunostained (ICC) ZO-1 in a selected Caco-2 clone validated the fidelity of tagged-ZO-1 for live cell tracking. Images are projections of maximum pixel intensity of apical z-stack images acquired with 1 μm depth and 0.3 μm intervals. Scale bar: 10 μm. (**C**) Images of apical mCherry-ZO-1 in live Caco-2 monolayer cultures in contact with nanostructured (NS) or flat (FT) polypropylene films for 0.5-1.5 hours at 37°C, and non-treated (NT) control. Cytosolic complexes larger than 1.0 μm diameter (white arrows) appeared at the apical side of cells in contact with a NS films. Images are projections of maximum pixel intensity of apical z-stack images acquired with 1 μm depth and 0.3 μm intervals. Scale bar: 10 μm. (**D**) Size distribution of apical cytosolic complexes (d ≥ 1.0 μm) in images represented in (C). (**E**) Number of (d ≥ 1.0 μm) complexes of each image in (C). Data are mean ± s.d. (n = 25 images for each treatment, from 5

488   independent experiments)*,* and *P* values were determined by one-way ANOVA. (**F**) Immunostained
489   images of mCherry-ZO-1 engineered Caco-2 cells after treatment with NS film at 37ºC for 1 hour show
490   co-localization of Claudin-10 and F-actin in cytosolic mCherry-ZO-1 complexes. Scale bar: 2 μm.
491
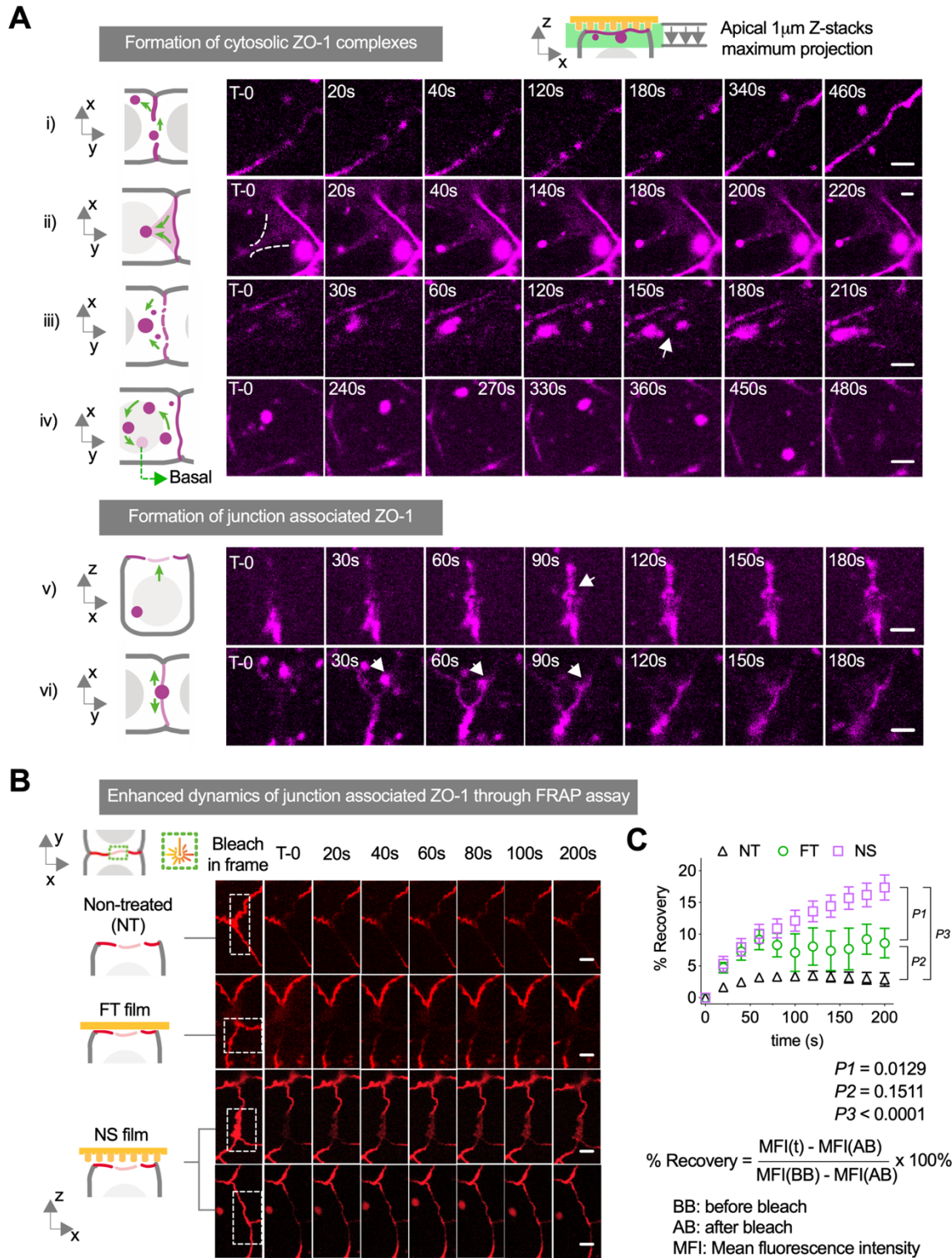
Fig. 3. Enhanced dynamics of junction-associated ZO-1 in engineered Caco-2 cells in contact with nanostructured film. (A) Time-lapse images of mCherry-tagged ZO-1 at the apical side of the cells stimulated by nanotopographic cues for 0.5-1.5 hour at 37°C. Means of cytosolic complexes formation included: i) junction-associated ZO-1 proteins aggregate and dissociate from the original structure into the cytosol; ii) cytosolic ZO-1 proteins cluster into puncta within a network (highlighted by white dashed line)

498 next to junctions; iii) cytosolic structures merge with newly restructured ZO-1; iv) apical cytosolic
499 complex circulates while collecting smaller ZO-1 structures which then moves basolaterally. Junction-
500 like ZO-1 structure formed through v) rapid reorganization likely originated from basolateral side; and vi)
501 direct transformation of cytosolic ZO-1 complex (white arrow). Images are projections of maximum pixel
502 intensity of apical z-stack images acquired with 1 μm depth and 0.3 μm intervals. Scale bar: 2 μm. (**B**)
503 Time-lapse images of junction-associated mCherry-ZO-1 after photobleaching at a selected region (white
504 dashed line) in response to contact with either a flat (FT) or nanostructured (NS) film for 0.5-1.5 hour or
505 that were non-treated (NT). Scale bar: 2 μm. (**C**) Quantification of fluorescence recovery after
506 photobleaching (FRAP) in selected frames represented in (B). Data are mean ± s.d. (analyzed from 26
507 images for NT, 11 images for FT, and 29 images for NS, pooled from 2 independent experiments), and *P*
508 values were determined by one-way ANOVA analysis of recovery at 200 s.
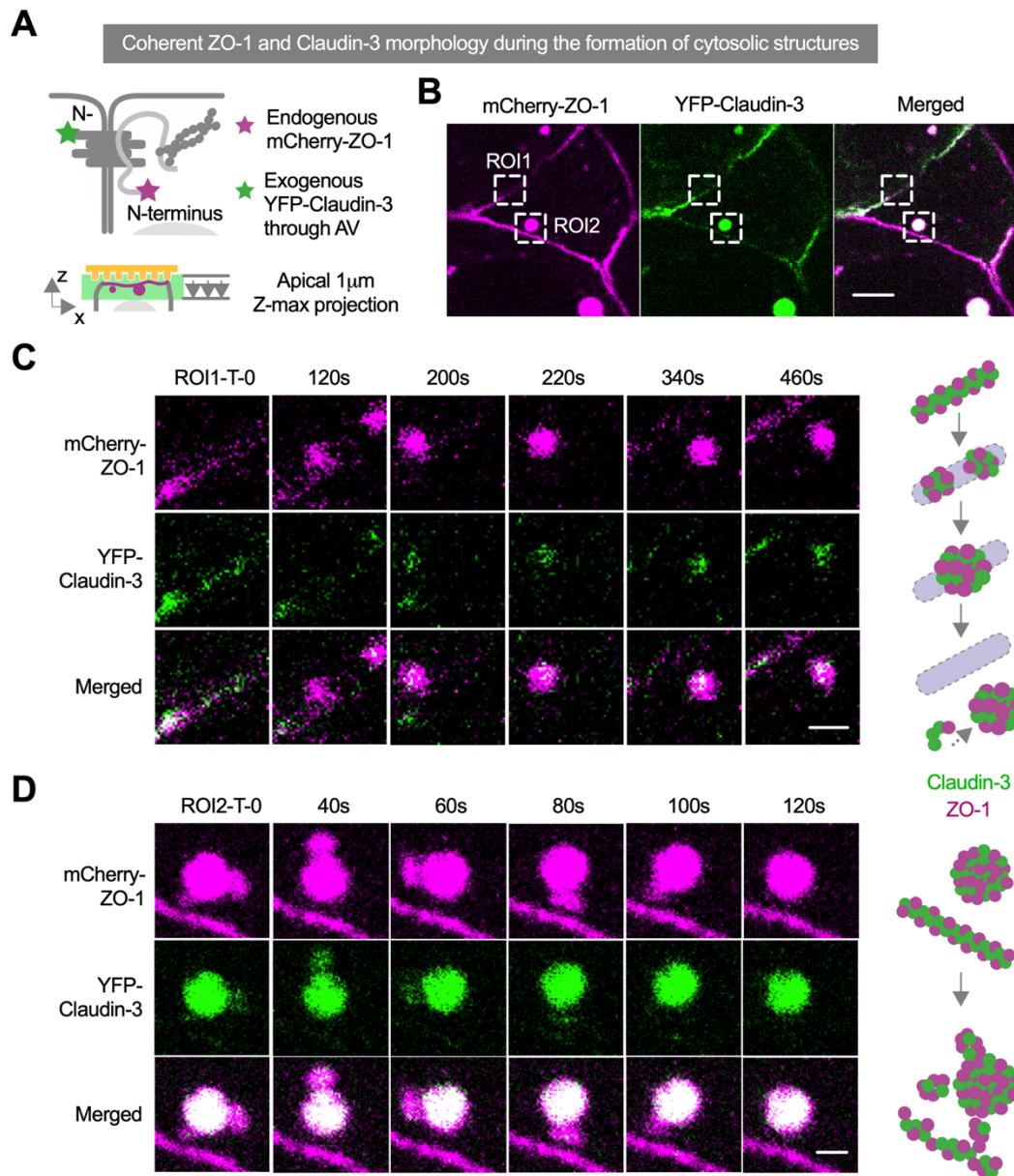
Fig. 4. Co-transport of ZO-1 and claudins during the initiation and formation of cytosolic complexes after nanotopographic contact. (**A**) Schematic of exogenous YFP-claudin3 adenovirus transduction in mCherry-ZO-1 engineered Caco-2 cells for live imaging analysis. Images of each time lapse were acquired at apical 1 μm depth with 0.3 μm intervals and projected the maximum pixel intensity into presented images. (**B**) Images of mCherry ZO-1 and YFP-claudin-3 co-expressing Caco-2 cells treated with a nanostructured film at 37ºC for 0.5-1.5 hour, showing co-localization of ZO-1 and claudin-3 in apical cytosolic complexes. Scale bar: 10 μm. (**C**) Time-lapse images of ROI1 in (B) show the involvement of both ZO-1 and claudin-3 in the initiation of complex formation and cytosolic migration. (**D**) Time-lapse images of ROI2 in (B) show formation of apical cytosolic complexes containing both ZO-1 and claudin-3 originating from a neighboring tight junction. Scale bar: 2 μm.
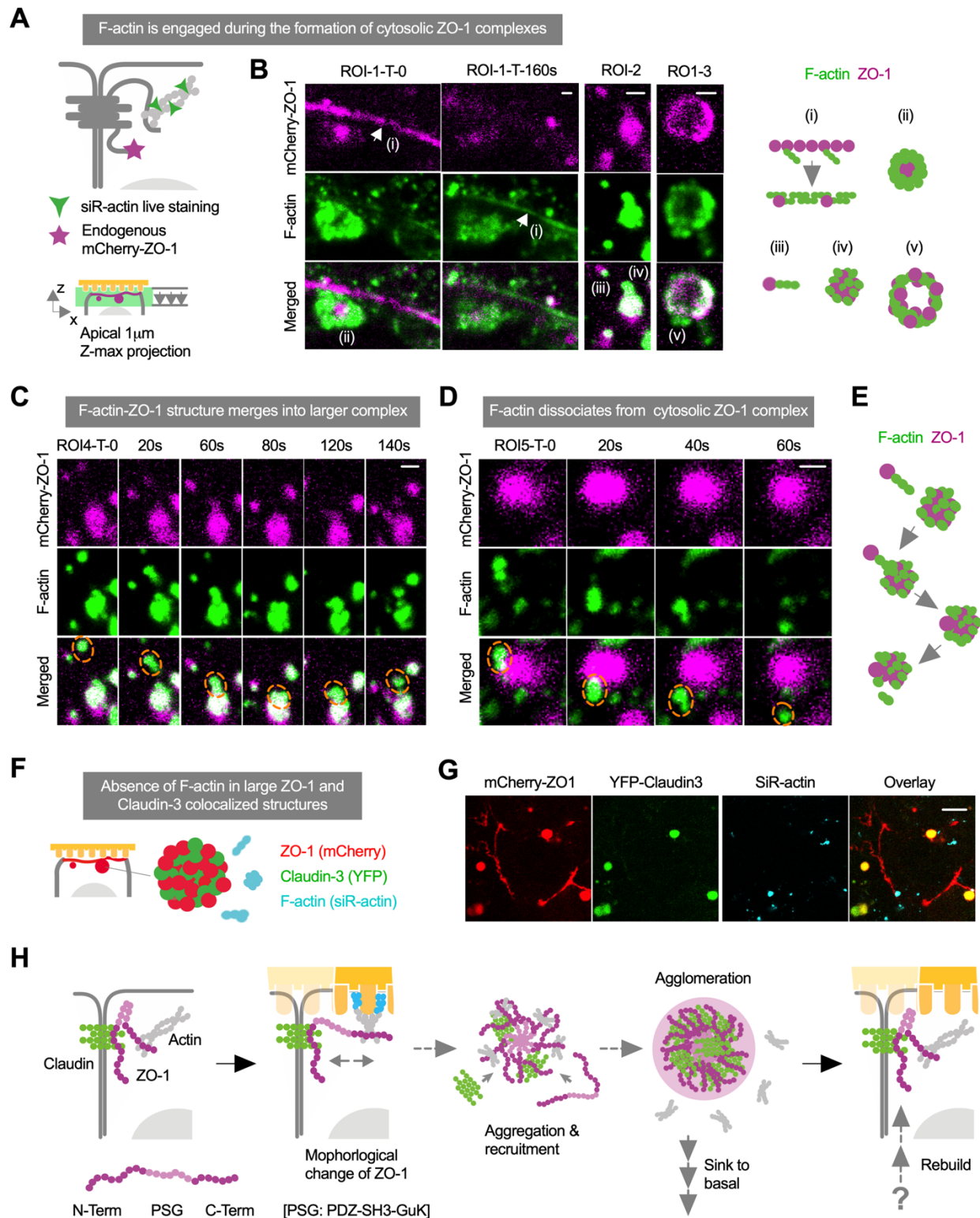
521
522
523 **Fig. 5. Nanotopographic modulation engages F-actin in the formation of ZO-1 cytosolic complexes.**
524 (**A**) Schematic of F-actin staining in mCherry-ZO-1 engineered Caco-2 cells for live imaging analysis.

525 Images of each time lapse are acquired at apical 1 μm depth with 0.3 μm intervals and projected the
526 maximum pixel intensity into presented images. (**B**) Images of cells stimulated by nanotopographic cues
527 for 0.5-1.5 hour at 37ºC show different patterns of F-actin/ZO-1 interactions: i) disappearance of ZO-1
528 concomitant with the appearance of F-actin at tight junctions; ii) F-actin wrapped around ZO-1 in cytosolic
529 complexes next to a tight junction; iii) polarized cytosolic F-actin-ZO-1 complexes with F-actin facing
530 toward iv) a larger solid integrated structure; and v) organization of F-actin and ZO-1 into large (>2 μm
531 diameter) hollow structures. Scale bar: 2 μm. (**C**) Time-lapse images show merging of the F-actin-ZO-1
532 structure (orange dashed line) into a larger complex containing the two proteins. Scale bar: 2 μm. (**D**)
533 Time-lapse images show dissociation of F-actin from cytosolic ZO-1 complex. Scale bar: 2 μm. (**E**)
534 Summary schematic of F-actin associated dynamics involved in formation of cytosolic ZO-1 complexes.
535 (**F**) Schematic of mCherry-ZO-1, YFP-claudin-3 and F-actin interactions in engineered Caco-2 cells for
536 live imaging analysis. (**G**) Images of live cells that are stimulated by nanotopographic cues for 72 mins at
537 37ºC show co-localization of ZO-1 and claudin-3 but not F-actin in apical cytosolic complexes. Scale bar:
538 10 μm. (**H**) Proposed mechanism of tight junction remodeling in response to nanotopographic cues
539 involving ZO-1 cytosolic complexes.
540

Supplementary Materials

Title: Nanotopography enhances dynamic remodeling of tight junction proteins through cytosolic complexes

Authors: Xiao Huang[1], Xiaoyu Shi[2,3], Mollie Eva Hansen[4], Cameron L. Nemeth[4], Anna Ceili[5], Bo Huang[2,6,7], Theodora Mauro[5], Michael Koval[8], and Tejal A. Desai[1,4*]

Affiliations:

[1] Department of Bioengineering and Therapeutic Sciences, University of California, San Francisco, San Francisco, California, USA

[2] Department of Pharmaceutical Chemistry, University of California, San Francisco, San Francisco, California, USA

[3] Department of Developmental and Cell Biology, University of California, Irvine, Irvine, California, USA

[4] UC Berkeley-UCSF Graduate Program in Bioengineering, University of California, San Francisco, San Francisco, California, USA

[5] Department of Dermatology, University of California, San Francisco, San Francisco, California, USA

[6] Department of Biochemistry and Biophysics, University of California, San Francisco, San Francisco, California, USA

[7] Chan Zuckerberg Biohub, San Francisco, California, USA

[8] Division of Pulmonary, Allergy, and Critical Care Medicine and Department of Cell Biology, Emory University School of Medicine, Atlanta, Georgia, USA

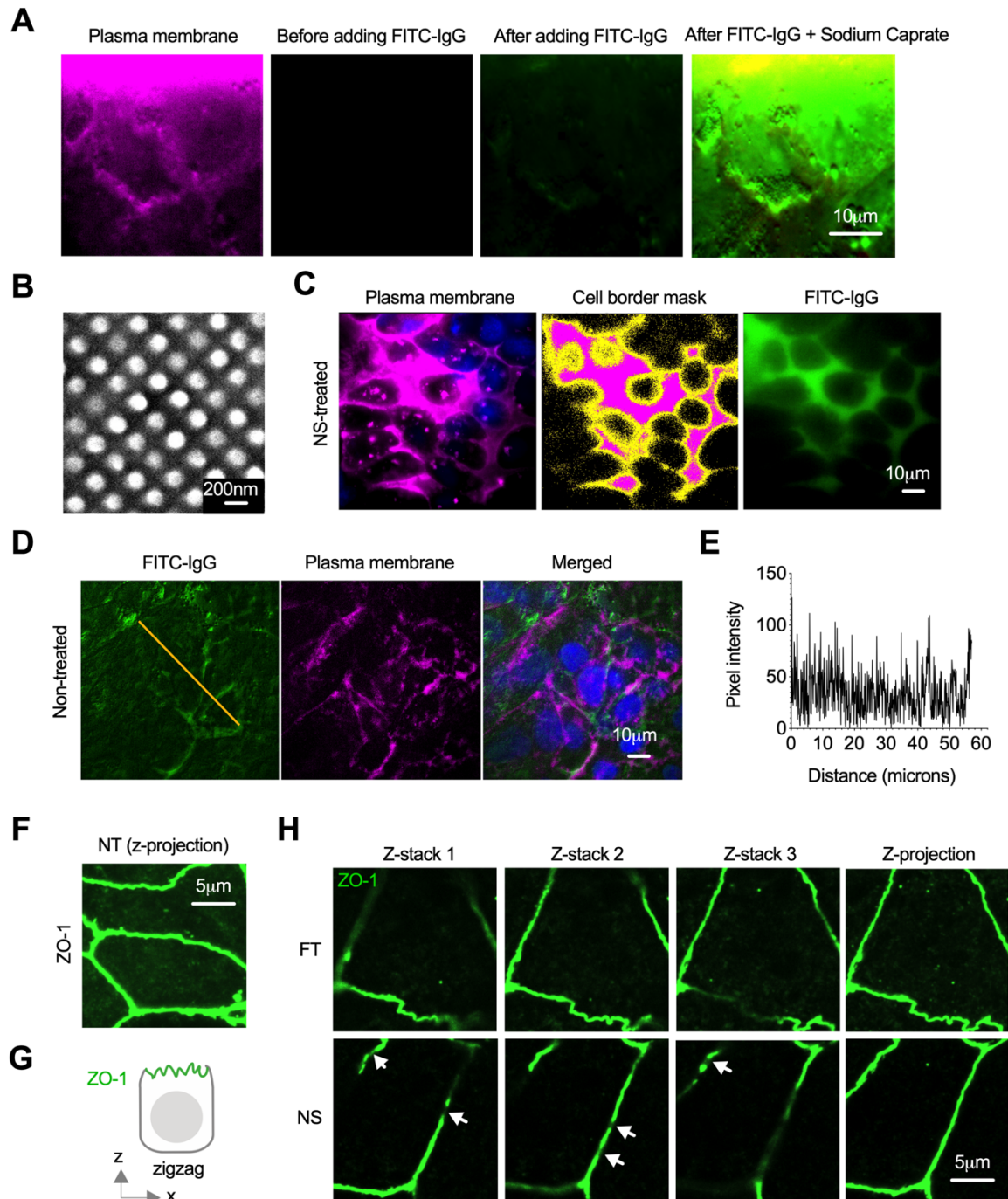*Correspondence to: Tejal A. Desai, PhD (email: tejal.desai@ucsf.edu)

Fig. S1. Enhanced leakiness of biomolecules through paracellular junctions with nanotopographic film treatment. (**A**) TIRF images of basal side of live Caco-2 monolayer treated with FITC-labeled IgG and sodium caprate, showing polarized epithelial monolayer with paracellular barriers blocking the penetration of macromolecules from apical side to basal side. Adding sodium caproate at 1 mM irreversibly opened tight junctions and led to immediate penetration of FITC-IgG through the monolayer to be detected by TIRF imaging at the basal side. (**B**) Scanning electron microscopy (SEM) image of nanostructured polypropylene film. (**C**) Images

of cell-cell border area mask generation from plasma membrane staining, which is used for quantification and normalization of FITC-IgG signal accumulation. (**D**) TIRF images of basal membrane of live epithelial cell Caco-2 monolayer treated with FITC-labeled IgG for 1 hour at 37°C (from n = 3 independent experiments). (**E**) Transverse profile of FITC-IgG as indicated by the lines in (D). Signal intensity and distribution in FITC-IgG channel is not comparable to the conditions where the flat/nanostructured film are in direct contact with cells (Fig. 1c) due to the reflection effect of the film during TIRF imaging. (**F**) Image of immunostained ZO-1 in non-treated Caco-2 cells, as compared to Fig. 1g&h. (**G**) Schematic of ZO-1 zigzag morphology at xz/yz focal plane of Caco-2 cells in direct contact with nanostructured film. (**H**) Images of immunostained ZO-1 in Caco-2 cells treated with NS or FT film for 1 hour at 37°C show zigzag morphology at xz/yz focal plane. Z-projection images are projections of maximum pixel intensity of z-stack images acquired with 6 μm depth and 0.3 μm intervals.
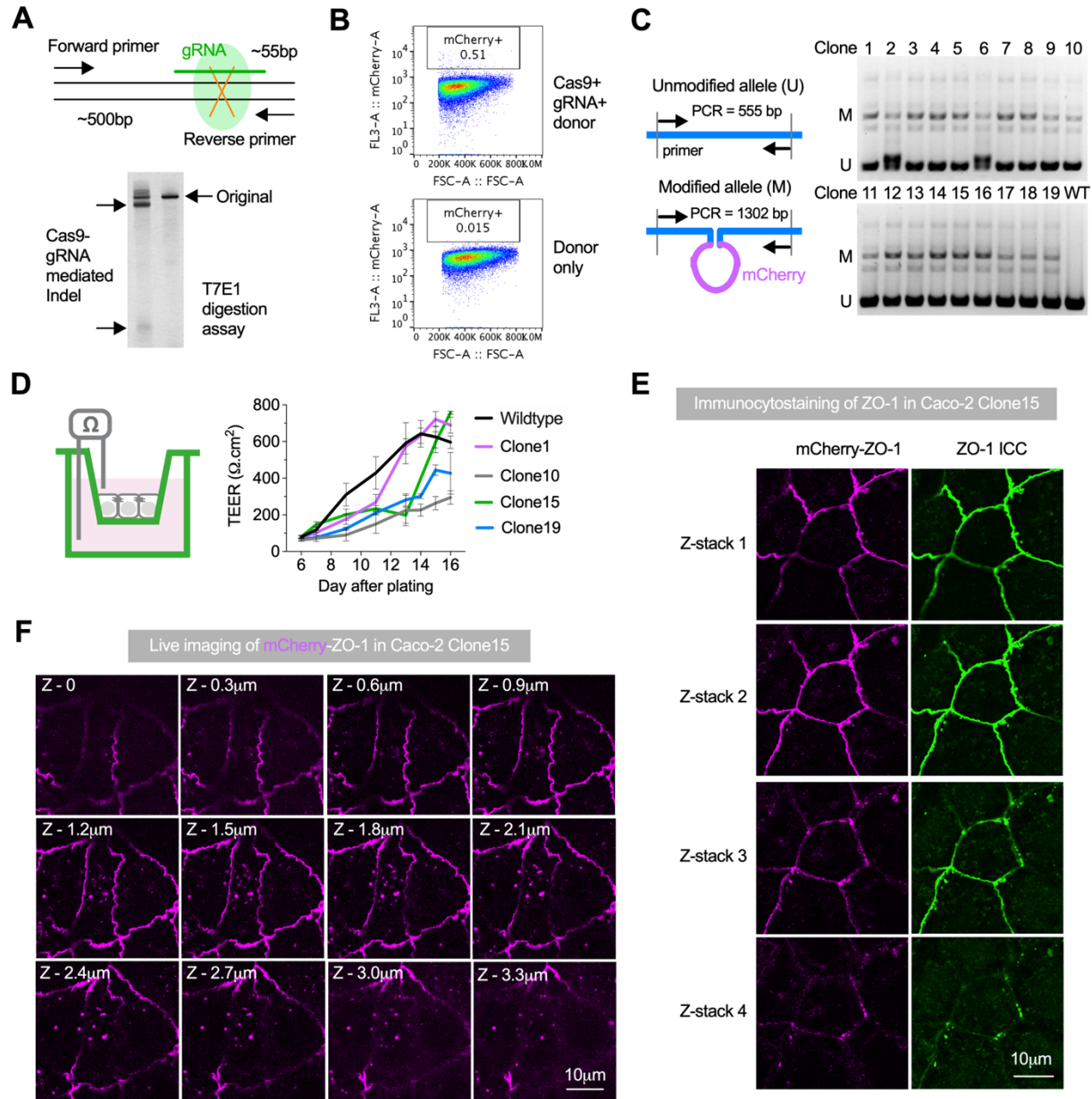
Fig. S2. Tagging of endogenous ZO-1 with mCherry reporter in Caco-2 cells through CRISPR-based genome editing and its phenotypic confirmations. (**A**) T7E1 digestion assay and agarose gel electrophoresis to detect Cas9-gRNA mediated insertion/deletion (indel) of targeted *TJP1* gene. (**B**) FACS sorting of CRISPR-transduced Caco-2 cells to enrich mCherry positive population (in frame). Top panel: forward scattering and mCherry signal plot of cells co-transfected with Cas9, gRNA and donor template DNA after 14 days; bottom panel: forward scattering and mCherry signal plot of un-transfected control cells. (**C**) Genomic PCR and agarose gel electrophoresis of purified clones to confirm the insertion of mCherry gene at intended loci. All of the isolated clones have heterozygous modification of ZO-1. (**D**) Validation of barrier formation potency of engineered Caco-2 clones through transepithelial electrical resistance (TEER) measurements of cells cultured on transwell inserts. Clone15 with optimal accumulation

of TEER values was selected for imaging analysis. Data are mean ± s.d. (n = 3 biological replicates). (**E**) Co-localization of mCherry and immunocytostaining (ICC) of ZO-1 in Caco-2 Clone15 at different Z-stacks. (**F**) Z-stack scanning of live Caco-2 Clone15 by confocal microscopy reveals cytosolic structures of ZO-1 at basal-lateral locations underneath tight junctions.
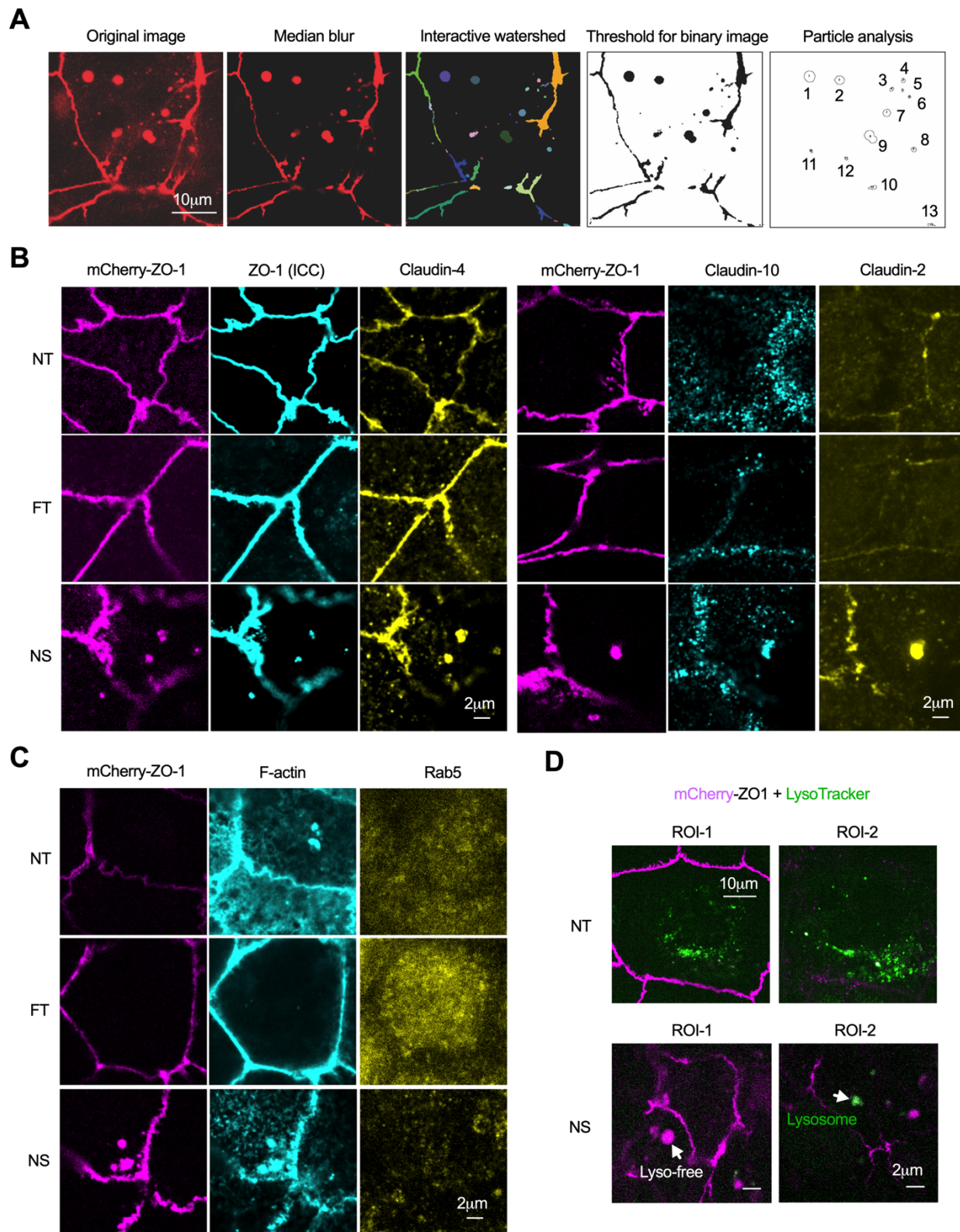
Fig. S3. Quantification and compositional identification of cytosolic ZO-1 complexes formed upon nanostructured film treatment. (A) Processing and quantification of cytosolic complexes

in images of engineered Caco-2 cell apical locations. Images were individually processed through median blur, interactive watershed, threshold for binary image and particle analysis. Size distribution of spherical complexes in images were reported in Fig. 2d,e. (**B,C**) Immunostained images of mCherry-ZO-1 engineered Caco-2 cells after treatment with NS film at 37°C for 1 hour showed co-localization of Claudin-2, Claudin-4, Claudin-10 (B) and F-actin (C) in cytosolic mCherry-ZO-1 complexes, while Rab5 was absent (C). (**D**) Images of LysoTracker dye stained live Caco-2 cells that were non-treated (NT) or in contact with NS film for 0.5-1.5 hour at 37°C showing that the apical cytosolic complexes are non-acidic. Scale bar: 2 μm.
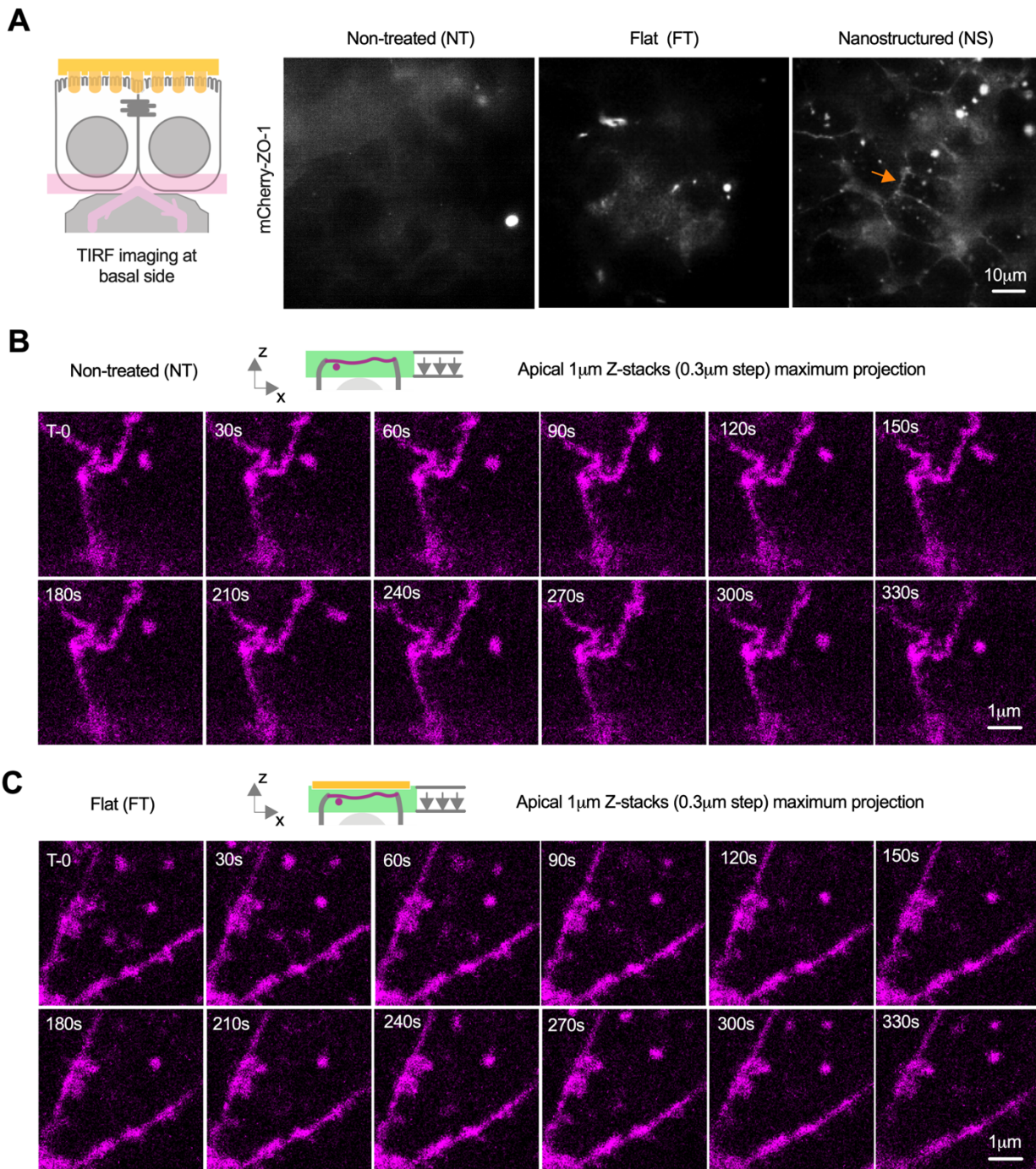
Fig. S4. Live imaging of engineered mCherry-ZO1 cells at apical and basal side upon different treatment. (**A**) TIRF images at the basal side of engineered Caco-2 cells that were non-treated, or treated with flat or nanostructured film at the apical side for 1 hour at 37ºC, showed interesting junction-like morphology (orange arrow) of mCherry-ZO-1 in cells stimulated by nanotopography. (**B,C**) Time lapse of apical mCherry-tagged ZO-1 in non-treated (NT) Caco-2 cells and those treated with flat film (FT) for 0.5-1.5 hour at 37ºC. Fewer and smaller cytosolic structures of ZO-1 at apical side were observed in NT (**B**) or FT (**C**)-treated cells, and the

interaction between tight junction and cytosolic structure was minimal. Images are projections of maximum pixel intensity of apical z-stack images acquired with 1 μm depth and 0.3 μm intervals.
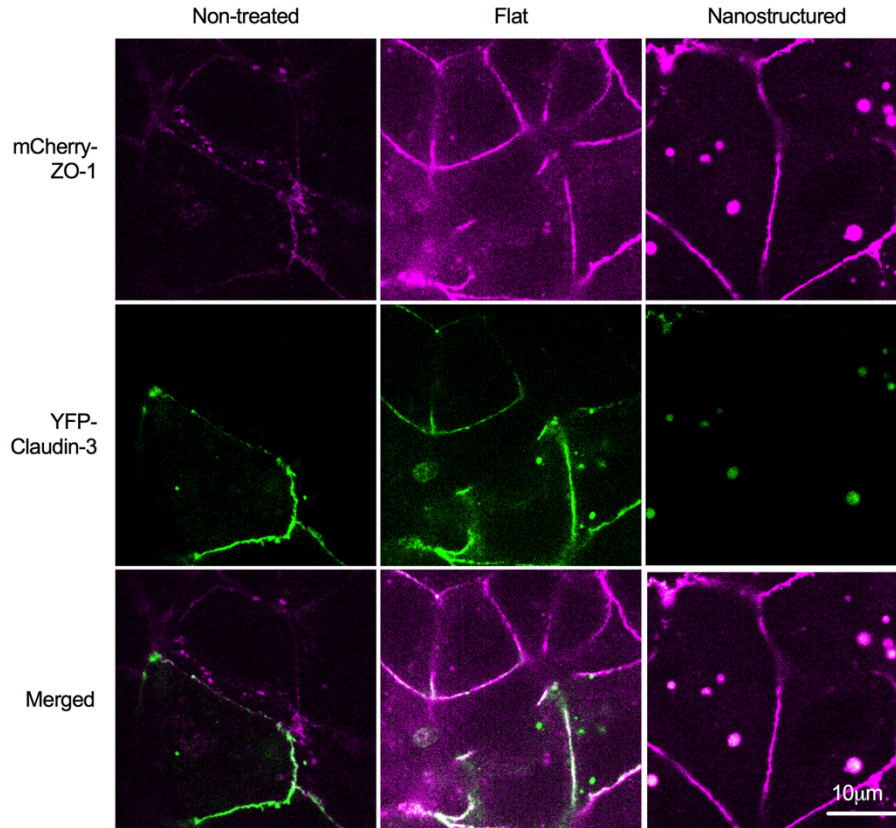
Fig. S5. Live imaging of engineered mCherry-ZO1 cells that are exogenously transfected with YFP-Claudin-3, in response to flat and nanostructured film in comparison with untreated control. Adenovirus transfection of Caco-2 cells was controlled at 100 MOI (multiplicity of infection) to minimize unnatural accumulation of cytosolic Claudin-3, while tolerating uneven expression level among cells. Nanotopographic treatment led to apical cytosolic complexes that contain both ZO-1 and Claudin-3; however, in untreated or flat film treated cells, smaller and fewer cytosolic structures did not contain both proteins.
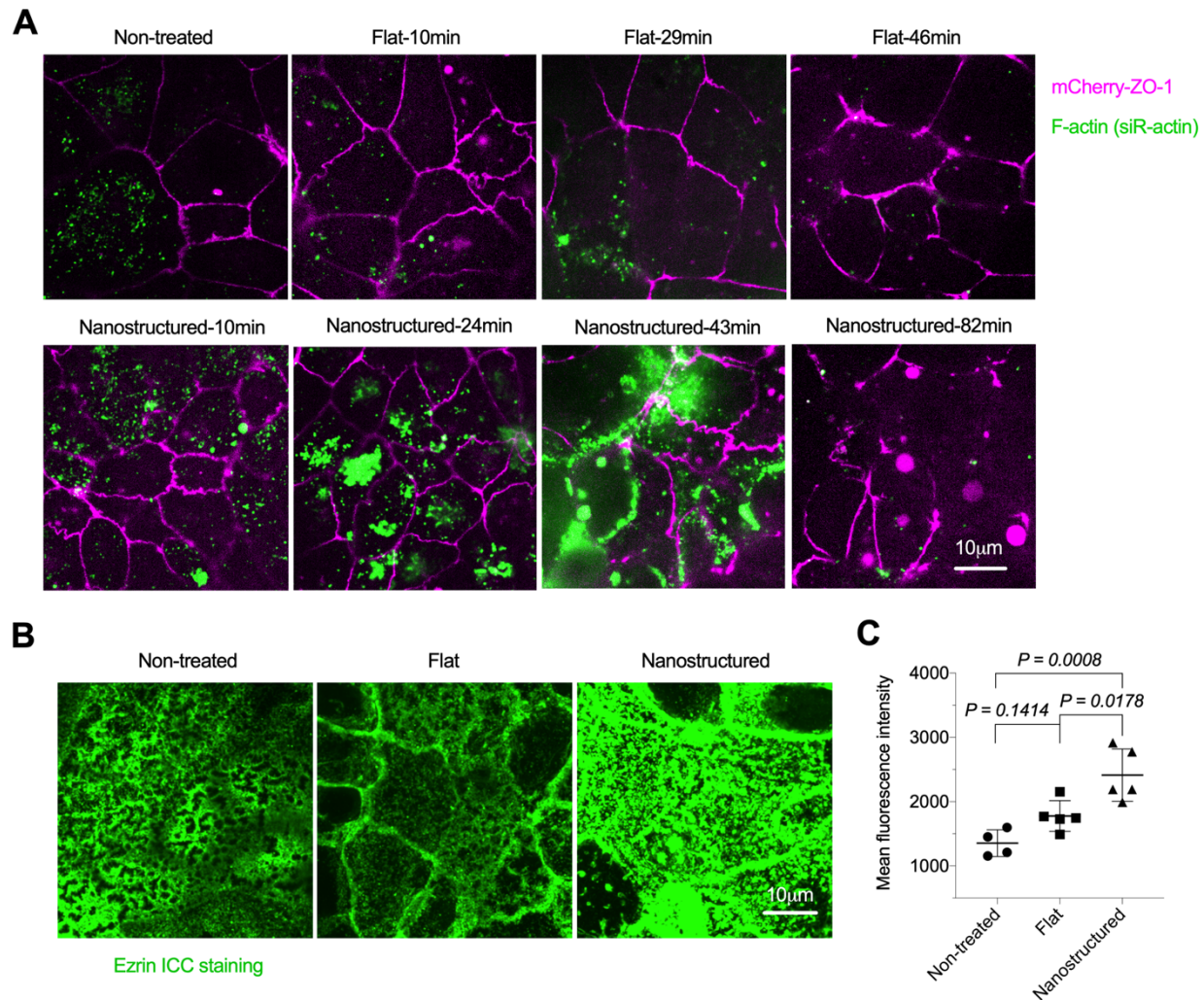
Fig. S6. F-actin clusters and remodels at apical side upon nanostructured film treatment, while ezrin protein, a connecter between cell membrane protein and actin, was up-regulated as well. (**A**) Images of F-actin stained live mCherry-ZO-1 cells at different time point after flat and nanostructured film treatment. Apparent clustering and remodeling of F-actin in live cell apical side was observed from nanostructured film treatment; however, this trend was less obvious from flat film treatment and even less for non-treated cells. Images are projections of maximum pixel intensity of apical z-stack images acquired with 1 μm depth and 0.3 μm intervals. (**B**) Images of ezrin staining of Caco-2 cells treated with flat and nanostructured film for 1 hour at 37°C, compared with non-treated control. Images are projections of maximum pixel intensity of apical z-stack images acquired with 6 μm depth and 0.3 μm intervals. (**C**) Quantification of mean pixel intensity in images shown in (B). Data are mean ± s.d. (n = 5 images), and *P* values were determined by one-way ANOVA analysis.

Note S1. Sequence of repair plasmid for HDR-based mCherry knock-in.

The following 2747bp gene was cloned in pUC57-Kan plasmid by EcoRV (Genscript, Inc).

aggagatcgagaccatcccggctaaaacggtgaaaccccgtctgtactaaaaatacaaaaaattagccgggcgtagtggcgggcgcctgtagtcccagctacttgggaggctgaggcaggagaatggcgtgaacccgggaggcggagcttgcagtgagccgagatcccgccactgcactccagcctgggcgacagagcgagactccgtctcaaaaaaaaaaaaaaaaTAATAATTTATTTTCCTCTCTATTGAGAGGCTCATGACAGGAGGTAAAACTGAAGTACGCTATAATTTGGGCAGGACCTGTATTGGAGCTCTTACTGCTTTTATTTTATGATGATTCTTGGGGGGAGTTTGGGAGATTGTTCTTTTTTGTTTTTGTTTCTTGTGTGTATCTACGTGTGTGATACATATACTAGAAAAGCTGTTCTTTTTCTTTTGGTTATAAATGAAGCTTGAGAAGTAATTCTGTAGCAAAACTGAAACTAGGTAGAGTAGTCATGTTTGTGACGTTAAAGCAGCCATTTGCCAAACCTATTAATGGTTTTATCTGTTTTCCTGTGACATGTATATTTATAATTACTGTGTTCAGAGGCATTTAACTTTCCCTTCGTTTGTAAAACATAAGAGATGCTTTTAAATGTTTACGTGCCATTAGATATTTTAAGATAATACCGCTCCAACTTTTATTCTTTTCTAAGTATAAAGTTGCAGAATTAGCTTGAATACTGATTTCAGCTTGCATGAAATGAATATAGAGCAGCTGTCCAAATTAAGTTAAAAACAAAGGAAGTTCCTGTGTGTCGTTTCCTGTCTCTTAAAAGCAAACAAAAAACTTTCCATAATTATTAAGGTCCTTTCAGAGTGTCTCTAATATTAACTGTGAATTTTGGTATTTTCAGTGTGCTGAATTGTTGGATGTTCTTGCTCACCTTATTAAGGACATTTTCTTAAAAGGTAAATGATTTGTTTTTCTTTTCCTTTATCAGAGCAC==T==GCC==ATG==T·TGAGCAAGGGCGAGGAGGATAACATGGCCATCATCAAGGAGTTCATGCGCTTCAAGGTGCACATGGAGGGCTCCGTGAACGGCCACGAGTTCGAGATCGAGGGCGAGGGCGAGGGCCGCCCCTACGAGGGCACCCAGACCGCCAAGCTGAAGGTGACCAAGGGTGGCCCCCTGCCCTTCGCCTGGGACATCCTGTCCCCTCAGTTCATGTACGGCTCCAAGGCCTACGTGAAGCACCCCGCCGACATCCCCGACTACTTGAAGCTGTCCTTCCCCGAGGGCTTCAAGTGGGAGCGCGTGATGAACTTCGAGGACGGCGGCGTGGTGACCGTGACCCAGGACTCCTCCCTGCAGGACGGCGAGTTCATCTACAAGGTGAAGCTGCGCGGCACCAACTTCCCCTCCGACGGCCCCGTAATGCAGAAGAAGACCATGGGCTGGGAGGCCTCCTCCGAGCGGATGTACCCCGAGGACGGCGCCCTGAAGGGCGAGATCAAGCAGAGGCTGAAGCTGAAGGACGGCGGCCACTACGACGCTGAGGTCAAGACCACCTACAAGGCCAAGAAGCCCGTGCAGCTGCCCGGCGCCTACAACGTCAACATCAAGTTGGACATCACCTCCCACAACGAGGACTACACCATCGTGGAACAGTACGAACGCGCCGAGGGCCGCCACTCCACCGGCGGCATGGACGAGCTGTACAAG==TCCGGAAGTGCTGGGAGCGCAAGCGGAAGCGGAGGCTCCGG====T==GAGGAAACAGCTATATGGGAACAACATACAGTGACGCTTCACAGGGTAAGTTTGTGTTGCAGTAAGTAATCTGTGTATAACTCAGGATACTGGCAGCTTTGAAAACAATAGAGGAAAGCCAGATGTCAGGAAGCCAGAGGGAGGAGGAAACTTTTTCTATATTCTTTTGTTTAAAATTAGAGTTACAATAATTTTTTATTAAGGTCAAAAGTGAGCATGATTACTTTTTCATATATCCTTTTGAGTATTTGCTGTTTTTATTCCTGACTTAAAAAGTGATTTGCTTTTAAAATTTTGAGTGATCAGATAAAAGACTCTGTACATTAGTATAAATTATTATAAACTGCTTCAACCTTTCTGAGTATATATGCATCCATTGTGGGAGTGAAGTTTGAAATTAAACCAGGTTGTATGCATAATAAAATCCTAAAAGATACTTAATTGATTTCAAACATGTTGACCCAAGCTGTTGCTTAAACAATTGCAGATGCGAGAAGAGAGATGAGTAGTAGTAAGAGATGAGTTCTTACTTGGTGGgactaagaactttgtccgaagtgagactgctatcaatttgaattctggttctgcctttctcttgctttagaaatggggaagtgattcagtcaccttcgaaaaccttggttttcacaagtttaaaatggAACAAGTTGACACCAGTTCATGCTTTACCAATTTGTAAAGTTAAGTGTCTCTCAAAATTCTCTTTCCTCTCTTTCAAGAGAGCTGAATCTACTGATTACTCCCTTTCTTAGAGAATGTATGGAAAGAGAGAATATTTAAATACTGGCCTTGCACTTTACACTTACTATTTCTACCAGCTATATCCATTATTAGGAAGATGGAAAGGGGAAAGAATCATGTTGCTGGACTCTGCCCCTGATTATCTCACGAATGTTTGGATCTGCACATAGTAGATAATGGGTAAATTAATTATTAAAAAATAGTTGTTTTTggctgggtgtggtggctcacgcct

==**Mutation to avoid "NGG" or gRNA cutting**==
mCherry gene
==**Spacer**==

Movie S1. Time-lapse movie of mCherry-tagged ZO-1 at the apical side of Caco-2 cells stimulated by nanotopographic cues, showing cytosolic ZO-1 proteins cluster into puncta within a network next to junctions. This movie represents images in Fig. 3A-ii.

Movie S2. Time-lapse movie of mCherry-tagged ZO-1 at the apical side of Caco-2 cells stimulated by nanotopographic cues, showing apical cytosolic complex circulates while collecting smaller ZO-1 structures which then moves basolaterally. This movie represents images in Fig. 3A-iv.

Movie S3. Time-lapse movie of mCherry-tagged ZO-1 at the apical side of Caco-2 cells stimulated by nanotopographic cues, showing active remodeling of cytosolic complexes and their interaction with junction-associated structures.

Movie S4. Time-lapse movie of mCherry-tagged ZO-1 (purple) and YFP-tagged claudin-3 (green) at the apical side of Caco-2 cells stimulated by nanotopographic cues, showing the involvement of both proteins in the initiation of complex formation and cytosolic migration. This movie represents images in Fig. 4C.

Movie S5. Time-lapse movie of mCherry-tagged ZO-1 (purple) and live-stained F-actin (green) at the apical side of Caco-2 cells stimulated by nanotopographic cues, showing: i) disappearance of ZO-1 concomitant with the appearance of F-actin; ii) F-actin wrapped around ZO-1 in cytosolic complex next to a tight junction; and iii) a large ZO-1 cytosolic complex lack of F-actin. This movie represents images in Fig. 5B.